

Supplemental Material

1. Field data

1.1 LiDAR and multibeam echosounder bathymetry

Topographic LiDAR were acquired for the entire Maltese Islands during a 5.5 h flight in February 2012 using an IGI LiteMapper 6800 system. The data have a cell size of 1 m and were collected as part of the project “Development of Environmental Monitoring Strategy and Environmental Monitoring Baseline Surveys” funded by ERDF-156.

Multibeam echosounder data were acquired offshore the eastern coast of the Maltese Islands during a number of expeditions (Micallef et al., 2013). These include:

- MEDCOR (2009), Kongsberg-Simrad EM-710, grid size of 5 m;
- RICS10 (2010), Kongsberg-Simrad EM-3002D, grid size of 1 m;
- DECORS (2011), Kongsberg-Simrad EM-710, grid size of 1 m.

Bathymetry was derived by accounting for sound velocity variations and tides, and by implementing basic quality controls.

1.2 Uncrewed Aerial Vehicle surveys

An Uncrewed Aerial Vehicle survey was carried out at Gnejna Valley in 2017 using a DJI Phantom 4 Pro drone. The drone was flown at an altitude of 100 m, speed of 5 m s⁻¹, and side

lap of 65-70%. Six ground control points were selected and their location determined by differential GPS. Orthophotos and digital elevation models (Figure S1) with a horizontal resolution of 10 cm/pixel were generated from the Unoccupied Aerial Vehicle data using Drone Deploy.

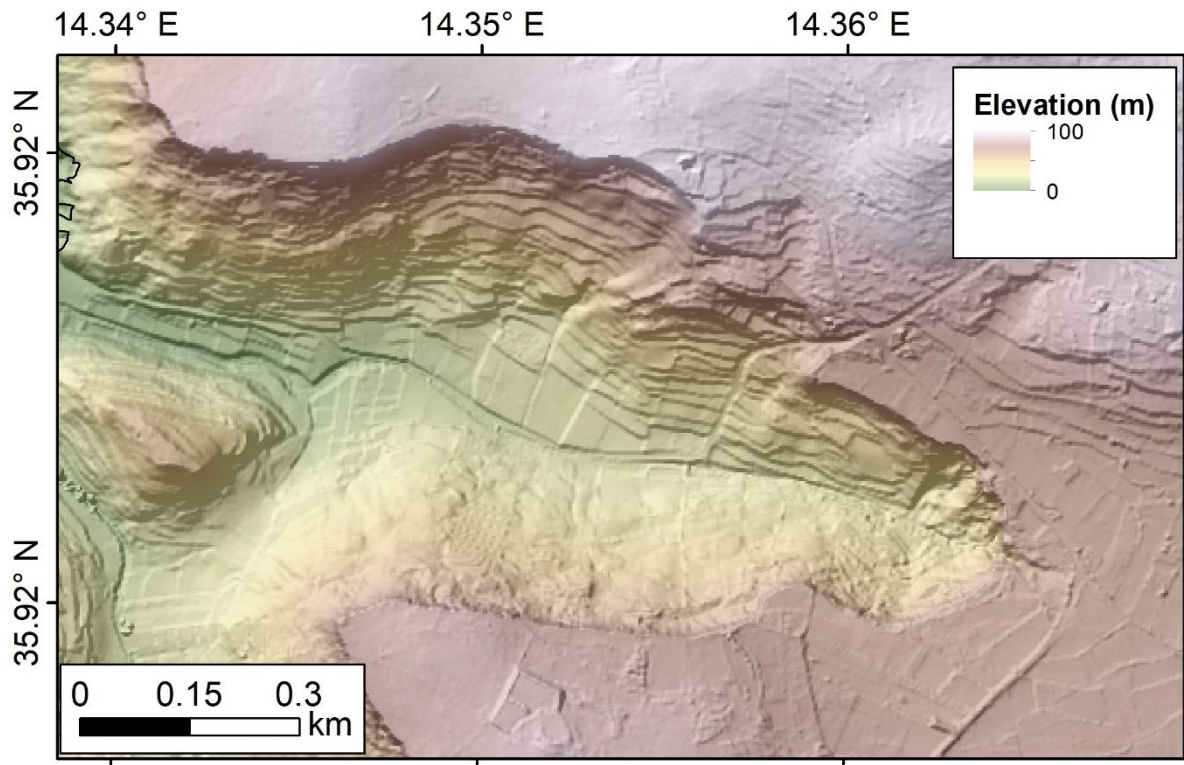


Figure S1: Digital elevation model of Gnejna Valley.

1.3 Site visits

Site visits were carried out at Gnejna Valley in 2017-2019. During these visits, geomorphic features of interest were noted and photographed, and samples were collected. The latter included ten surface samples from the wall at the head of the valley (Tal-Pitkal and Mtarfa Members) for Scanning Electron Microscopy (SEM), three small cores from the head of the valley (Tal-Pitkal and Mtarfa Members, Blue Clay Formation) for geotechnical and hydraulic

property measurement, and two Tal-Pitkal Member samples from the northern valley rim for cosmogenic nuclide dating.

1.4 Near-surface geophysical surveys

Electrical Resistivity Tomography (ERT) data were acquired along two 470 m long profiles by using a georesistivimeter Syscal (IRIS instrument) in the Wenner-Schlumberger configuration, with 48 channels and an electrode spacing of 10 m, in order to obtain an investigation depth of ~70 m. The profiles were located east of the Gnejna Valley head (profile T4) and to north of its northern rim (profile T1). The apparent resistivity data were processed and inverted into real resistivity values using two combined algorithms: Marquardt method (Marquardt, 1963) and Occam inversion (Constable et al., 1987) by the software ZondRes2D (Zond Geophysical software). Inversion took into account the local topography.

The ERT profiles were also surveyed with a Ground Penetrating Radar (GPR) investigation using a SIR3000 (Geophysical Survey Systems Incorporation). A 40 Mhz antenna and a two-way time range of 550 ns were used. The data were processed with the Reflex-W software (Sandmeier, <https://www.sandmeier-geo.de>). The GPR survey was carried out in 50 m segments. The first step of the processing flow was Distance Normalisation and the collage of consecutive profiles. The second step consisted of the application of a bandpass filter (10-100 Mhz), background removal and the application of a gain function, in order to highlight the deep signals. Diffraction hyperbolae were used to estimate the mean electromagnetic wave velocity (0.04 m/ns), which was used for depth conversion (20-22 m).

The ERT and GPR profiles for T1 and T4 are shown in Figures S2 and 2G, respectively.

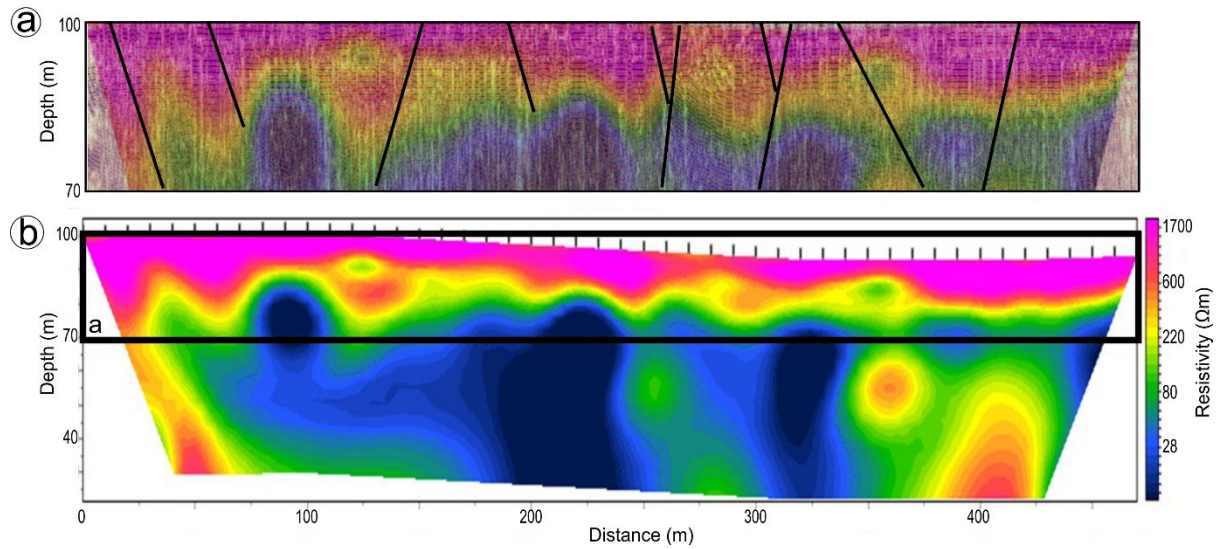


Figure S2: The (a) GPR and (b) ERT profiles for T1. Interpreted master joints and fractures are denoted by black solid lines in figure a. Location in Figure 1B.

2 Sample analyses

2.1 Scanning Electron Microscopy (SEM)

A sub-sample $5 \text{ mm} \times 5 \text{ mm}$ in area was taken from the surface of each SEM sample and dried in an oven for six days at 100°C . The sub-samples were then carbon-coated and placed in the chamber of a Carl Zeiss Merlin Field Emission SEM.

2.2 Geotechnical and hydraulic property measurements

The geotechnical and hydraulic properties of the Upper Coralline Limestone and Blue Clay samples (Table S2) were measured according to the standards shown in Table S1. To determine strength parameters, at least 10 single-impact readings across an area of 1 m^2 were taken with the N-type Schmidt hammer at a distance interval of 5 m along the head of Gnejna Valley.

Table S1: Standards used for the measurements of geotechnical and hydraulic properties.

Geotechnical and hydraulic properties		Standard test
Upper Coralline Limestone	Young's modulus	ASTM D3148 - 02
	Poisson's ratio	ASTM D3148 - 02
	Bulk density	ASTM C127-07
	Joint friction angle	(Barton and Choubey, 1977; ISRM, 1978, 1985)
	Joint roughness coefficient	
	Joint compressive strength	
	Porosity	ASTM D2216 - 19
	Hydraulic conductivity	UNI CEN ISO/TS 17892-11
Blue Clay	Bulk density	ASTM D7263 - 21
	Cohesion	ASTM D 7181
	Friction angle	ASTM D 7181
	Hydraulic conductivity	UNI CEN ISO/TS 17892-11
	Moisture content	ASTM D 2216-92

Table S2: Geotechnical and hydraulic properties measured for the Tal-Pitkal and Mtarfa Members (Upper Coralline Limestone) and Blue Clay Formation.

Property	Units	Tal-Pitkal Member	Mtarfa Member
Young's modulus	GPa	7.2	4.7
Poisson's ratio	-	0.15	0.27
Bulk density	kN m ⁻³	25.39	17.25
Joint direction	°	287	280
Joint spacing	m	4.9	4.7
Joint friction angle	°	32.3	35.9
Joint roughness coefficient	kPa	11.1	13.3
Joint compressive strength	kPa	18.3	12.1
Porosity	%	0.6	17
Hydraulic conductivity	m s ⁻¹	5.0×10^{-12}	5.0×10^{-7}
Blue Clay Formation			
Bulk Density	kN m ⁻³	18.33	
Cohesion	kPa	38	
Friction angle	°	22	
Hydraulic conductivity	m s ⁻¹	5.9×10^{-11}	
Moisture content	%	26.6	

The spacing of discontinuities (joints, fault-related fractures) measured during the scanline survey is shown in Figure S3.

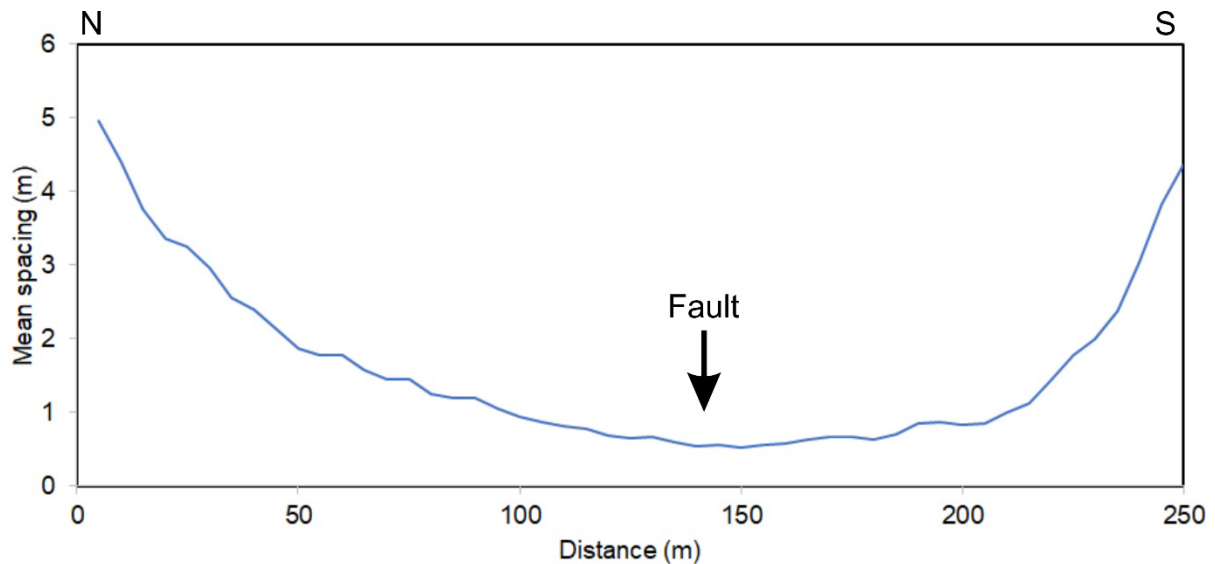


Figure S3: Trendline (moving average) of measured discontinuity spacing along the head of Gnejna Valley.

2.3 Cosmogenic nuclide dating

Samples 01 and 02 from the Tal-Pitkal Member (Table S3) were processed at the New Mexico Institute of Mining and Technology ^{36}Cl preparation laboratory. Samples were crushed and sieved to 0.15-1 mm and then leached. The dried sample was split using the cone and quarter technique. One split of each sample was powdered and sent to SGS Canada for major and trace element analysis by XRF, ICP-AES, and ICP-MS (Table S4). Approximately 32 g from a second split was measured and transferred to a Teflon bottle with 18 mΩ water then combined with ~3 g of ^{35}Cl spike. The 85.99% spike solution is a mixture of isotopically enriched NaCl (99.96% ^{35}Cl) and natural NaCl (75.77% ^{35}Cl). The samples were dissolved in concentrated HNO_3 for several days, after which AgNO_3 was added to precipitate AgCl . A blank, comprised of similar amounts of ^{35}Cl spike, 18 mΩ water and HNO_3 , was processed alongside the rock samples to estimate background ^{36}Cl (Table S5). The AgCl was then dissolved with NH_4OH and reprecipitated with HNO_3 in order to purify the sample. The AgCl was again dissolved and

BaNO₃ added to precipitate BaSO₄, removing any sulfur-36, a potential source of isobaric interference. The solution was filtered, AgCl precipitated, dried and sent to PRIME Lab at Purdue University to be analysed by Accelerated Mass Spectrometry.

Table S3. Location and physical attributes of samples

Sample ID	Lat. (dec. deg.)	Long. (dec. deg.)	Elev. (m)	Atm. pressure (hPa)	Topographic shielding	$\Lambda_{f,e}$ (g/cm ²)	Thickness (cm)
01	35.9222	14.3466	85	1006	0.6776	154	5
02	35.9223	14.3496	73.8	1007	0.5683	154	5

$\Lambda_{f,e}$ = effective attenuation length.

The CRONUScalc exposure age calculator calculates atmospheric pressure from latitude, longitude, and elevation using the ERA-40 model of the atmosphere (Marrero et al., 2016b; Uppala et al., 2005).

Table S4. Whole rock composition of ^{36}Cl samples.

Sample ID	01	02
Major elements (wt. %)		
SiO_2	0.97	1.07
TiO_2	0.02	0.02
Al_2O_3	0.36	0.40
Fe_2O_3	0.27	0.24
MnO	0.01	0.00
MgO	0.36	0.38
CaO	54.05	55.24
Na_2O	0.01	0.01
K_2O	0.02	0.02
P_2O_5	0.02	0.02
LOI	43.40	43.40
Total	99.48	100.79
Trace elements (ppm)		
B	<10	<10
Sm	NA	NA
Gd	NA	NA
U	0.60	0.47
Th	0.29	0.29
Cr	4.68	5.73
Li	1.58	1.62

Table S5. Chlorine content and chlorine isotopic compositions of blank

Sample ID	Spike mass (g)	HNO_3 (ml)	$^{35}\text{Cl}/^{37}\text{Cl}$ ^a	$^{36}\text{Cl}/10^{15} \text{ Cl}$ ^a	Cl content (10^{16} atoms Cl / mL HF) ^b	^{36}Cl (10^5 atoms) ^b
Blank	3.0254	61	5.94 ± 0.03	55.80 ± 2.96	7.152 ± 0.002	2.06 ± 0.02

^a Measurements from PRIME Lab^b Calculated using CRONUScale matlab code

Total Cl, $^{36}\text{Cl}_{\text{rock}}$ and their associated uncertainties were calculated from measured $^{36}\text{Cl}/\text{Cl}$ and $^{35}\text{Cl}/^{37}\text{Cl}$ ratios (Table S6) using isotope dilution mass spectrometry and by subtracting blank concentrations (Desilets et al., 2006; Marrero et al., 2016a). Exposure ages and topographic

shielding coefficients were computed using the online CRONUS ^{36}Cl Surface and Topographic Shielding calculators (<http://cronus.cosmogenicnuclides.rocks/2.1/>). Shielding was calculated from measurements of the samples' surface dip direction and angle, and the angle to the height of surrounding topography at numerous points along the 360° view from the sample location. Rock water contents were determined analytically through loss of ignition (LOI) at SGS and the bulk density, 2.6 g/cm^3 , was determined by this study. The pore water content was determined by weighing and oven-drying pieces of bulk rock sample. Due to distance of samples' location below the top of the cliff, the high Ca content of samples (which leads to ^{36}Cl production dominated by spallation) and their simple exposure history, ^{36}Cl inheritance is considered negligible.

Table S6. Chlorine content and chlorine isotopic compositions of samples.

Sample ID	Sample mass (g)	Spike mass (g)	HNO_3 (ml)	$^{35}\text{Cl}/^{37}\text{Cl}$ ^a	$^{36}\text{Cl}/10^{15} \text{ Cl}$ ^a	Cl (ppm) ^b	^{36}Cl (10^5 atoms/g) Blank-corrected ^b	Exposure age (ka)
01	32.4365	3.0253	61	5.73 ± 0.01	99.28 ± 3.18	9.7 ± 2.1	1.53 ± 0.01	11.1 ± 1.1
02	32.3400	3.0068	61	5.79 ± 0.01	167.61 ± 4.21	6.7 ± 2.1	3.79 ± 0.02	33.4 ± 3.4

^a Measurements from PRIME Lab

^b Calculated using CRONUScalc MATLAB code

Exposure age calculated using Lal/Stone scaling (Stone, 2000)

—
—

3 Modelling

3.1 Hydrological modelling

The mean annual precipitation and evapotranspiration coefficient for the Maltese Islands are ~550 mm (Galdies, 2011) and ~70% (FAO, 2006), respectively. The area of the catchment contributing surface runoff to the head of Gnejna Valley was estimated at 3854966 m² using the LiDAR data and hydrology tools in ArcMap (Figure 1A). The land cover across the catchment is predominantly agricultural land with natural vegetation (Copernicus, 2018), which was assigned a run-off coefficient of 50% (Schwartz and Zhang, 2003). Based on all this information, the volumes of surface runoff and groundwater infiltration across the Gnejna Valley catchment was estimated at 318034 m³ in one year.

Based on the Gnejna Valley geometry, the discharge that would be required to move Upper Coralline Limestone boulders with a diameter of 1.5 m was estimated. The critical shear stress for transport (τ_c) is based on the Shields equation:

$$\tau_c = \theta(\rho_s - \rho_w)gD \quad (1)$$

where θ is the Shields coefficient, ρ_s is the density of the rock, ρ_w is the density of water, g is gravitational acceleration, and D is the boulder diameter.

Assuming steady and uniform flow, the bed shear stress τ is:

$$\tau = \rho_w g R S \quad (2)$$

where R is the hydraulic radius (cross-sectional area divided by wetted perimeter), and S is the slope (in m/m).

Using a θ of 0.045 (for large particle Reynolds number (Komar, 1988)), ρ_s of 1700 kg m^{-3} , S of 0.03 (measured from LiDAR data) and D of 1.5 m, R needs to be >1.56 for the boulder to be mobilised.

Using the continuity and Manning equations:

$$Q = AV \quad (3)$$

$$V = R^{2/3} S^{1/2} n^{-1} \quad (4)$$

where Q is discharge, A is cross-sectional area of stream, V is the mean velocity and n is the Manning roughness coefficient (here taken as $0.2 \text{ s m}^{-1/3}$ (Chow, 1959; Phillips and Tadayon, 2006)), we estimate that V needs to be 1.16 m s^{-1} to transport the boulder. Such a velocity would be associated with a stream with a depth of 1.58 m and a discharge of $458 \text{ m}^3 \text{ s}^{-1}$ (for a valley with a width of 250 m like Gnejna valley). Such a discharge is equivalent to a precipitation intensity of 10.3 m per day.

If all the annual precipitation were to fall in one day at Gnejna Valley, and assuming that all the precipitation is transformed into run-off, the discharge of the stream generated would only be $25 \text{ m}^3 \text{ s}^{-1}$. Surface flow is therefore not responsible for the transport of 1.5 m wide boulders

in Gnejna Valley. The largest amount of rainfall recorded in one day is 100 mm (Galdies, 2011). The largest boulder that can be transported during such an event is ~ 0.1 m in diameter.

3.2 Modelling of surface erosion by overland flow

We consider a Landscape Evolution Model (LEM) based on Chen et. al. (2014). The model accounts for geomorphodynamic evolution through surface water run-off, surface erosion and stream incision, hillslope evolution (creep), karst denudation, and transport and deposition of eroded sediment mass.

To develop the governing equations, we consider a physical system composed of two main components - water and sediment - separated by an interface that we call the 'land surface'. The dynamic landscape is characterised by defining a time-dependent distribution of total landscape altitude $\theta(x, t) := l(x, t) + h(x, t)$ over a geographic plane $\Omega \in \mathbb{R}^d$ of dimension $d = \{1, 2\}$, where $l(x, t)$ is the land surface elevation, and $h(x, t)$ is the local height of the water column.

Water velocity over the land surface, $v(x, t)$, can be approximated using the generalised Gauckler-Manning relationship (Chen et al., 2014):

$$v = -h^\alpha \|\nabla \theta\|^{-\beta} \nabla \theta \quad (5)$$

The main governing equations include local mass conservation for water (6), intact sediment (7), and the sediment load in water (8):

$$\partial_t h + \nabla \cdot h v = r(x, t) \quad (6)$$

$$\partial_t l - \nabla \cdot c(l, x, t) \nabla l = -\epsilon(h, \|\nabla \theta\|, x, t) + \delta(\gamma, x, t) - \kappa(\|\nabla \theta\|, x, t) \quad (7)$$

$$\partial_t h \gamma + \nabla \cdot h \gamma v = \epsilon(h, \|\nabla \theta\|, x, t) - \delta(\gamma, x, t) \quad (8)$$

where r is the rate of water exchange with the atmosphere (e.g., through rainfall and evapotranspiration), ϵ is the rate of erosion, δ is the rate of sediment deposition, and κ is the rate of karst denudation. The term $(c \nabla l)$ describes the hillslope creep, which is a diffusive process with a smoothing effect over the landscape features over time. Finally, $\gamma(x, t)$ is the fraction of sediment per unit water column. Note that in the derivation of the governing equations 6-8, the compressibility of the phases has been ignored.

The erosion rate is parameterised using a stream incision law (Chen et al., 2014), as:

$$\epsilon = \begin{cases} e_0(x) h^m (\|v\| - v_{cr})^n & \text{if } \|v\| - v_{cr} > 0 \\ 0 & \text{if } \|v\| - v_{cr} \leq 0 \end{cases} \quad (9)$$

where, the parameter e_0 is the erosion rate constant, v_{cr} is the critical water velocity at which erosion initiates, and the exponents m, n are the stream-incision parameters.

The rate of deposition of the eroded soil mass is parameterised using Exner's law (Chen et al., 2014), as:

$$\delta = d_0(x) \gamma^p \quad (10)$$

where, the parameter d_0 is the deposition rate constant, and exponent p controls the 'holding' capacity of the water column.

Finally, the rate of karst denudation is modelled after Kaufmann et. al. (2001), as:

$$\kappa = k_0(x)(\|v\| - v_{cr}) \quad (11)$$

where, k_0 is the denudation rate constant.

The model was numerically discretised using a standard Galerkin finite element method with second order polynomials. A fully implicit Euler method was used for time discretisation. The resulting fully coupled discrete model was linearised using a classical Newton scheme and the linear system was solved using a stabilised Algebraic Multi-Grid (AMG) parallel solver. The numerical scheme was implemented within C++ based DUNE PDElab, which is a modular tool-box for solving partial differential equations (Sander, 2020).

The test setting, including the initial topography and the model parameters, is shown in Figure S4. This test domain is discretised into 100×50 elements, and the simulation is run for a period of 20000 years. Snapshots of the evolving landscape are shown in Figure S5. The flow of water at the cliff's edge develops a retrograding valley with a pointed head.

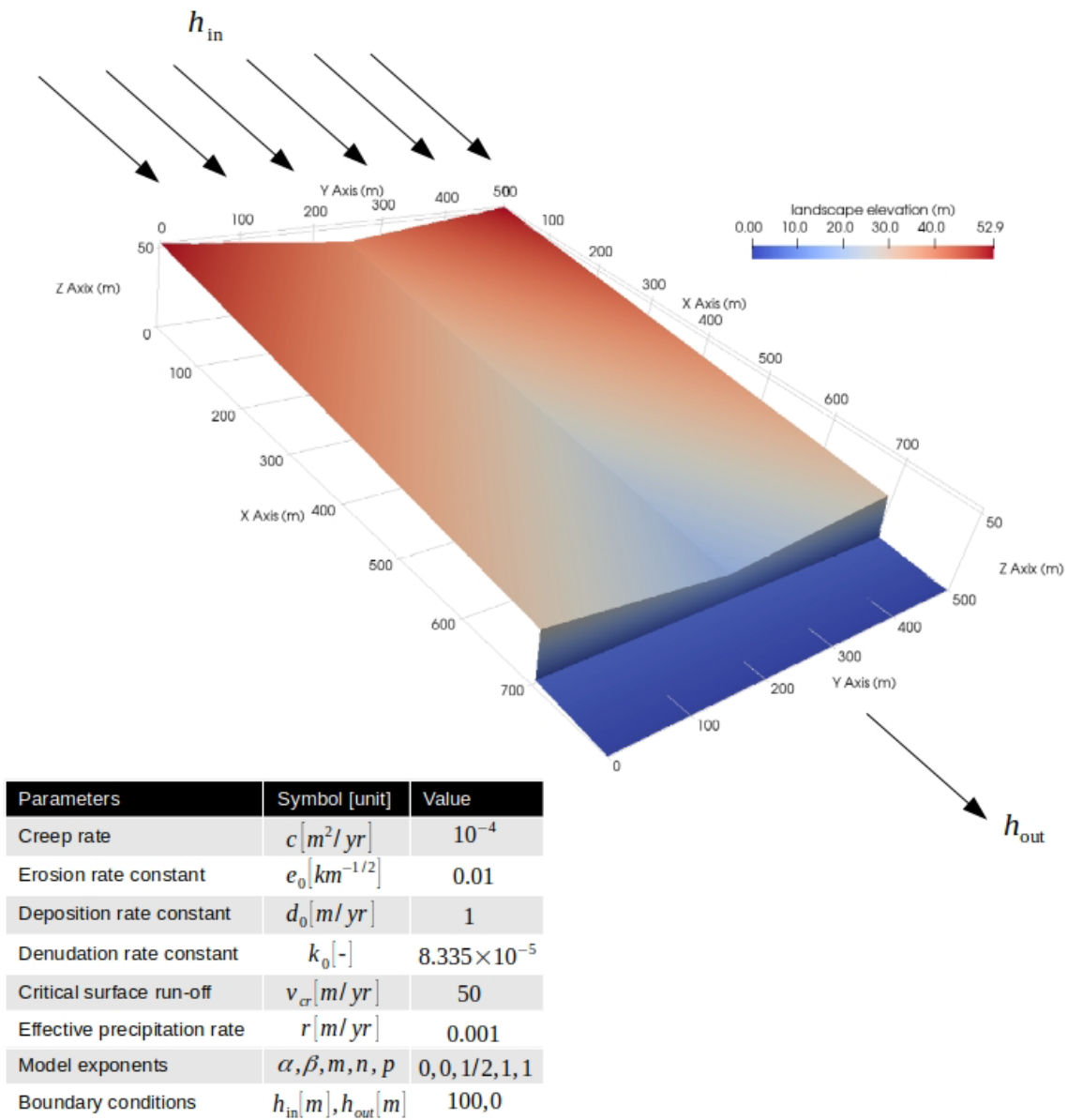


Figure S4: Test setting showing initial topography and the material parameters (based on Chen et al. (2014)).

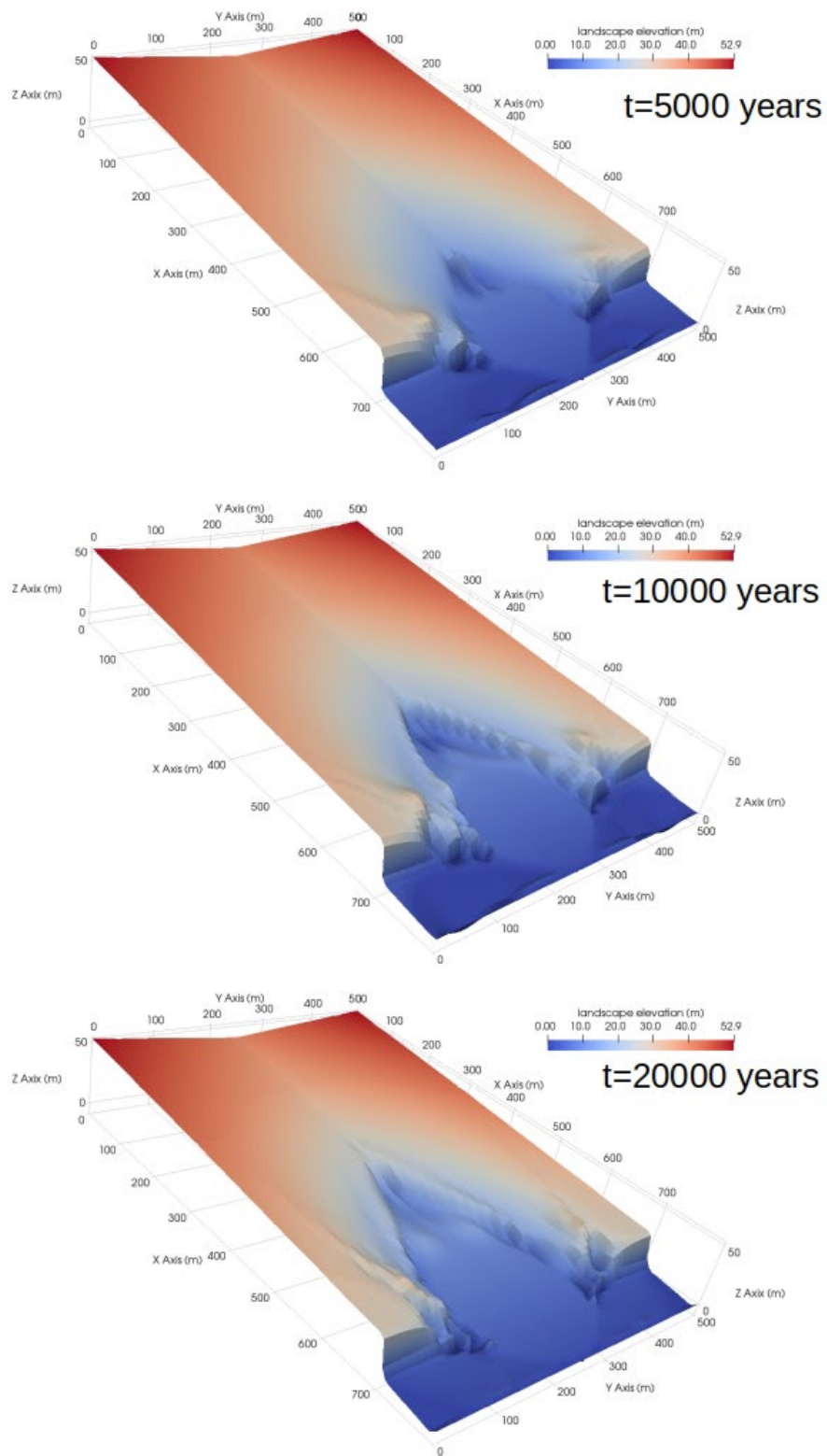


Figure S5: Snapshots of evolving landscape at 5000, 10000, and 20000 years.

3.3 3-D Distinct Element Modelling

The commercially available software 3DEC (<https://www.itascacg.com/software/3dec>) was used to develop a 3-D Distinct Element Model. The model consists of discrete, interacting blocks represented as polyhedrons with planar boundaries that correspond to joints in a rock mass. The blocks are assumed to be deformable and are internally discretised into finite-difference tetrahedral elements. Fluid and fluid pressure propagate through the model and equations of motion are solved using an explicit solution scheme. 3DEC uses a finite volume formulation for calculating stress, strain and displacement.

a. Governing equations

Fluid flow in rock discontinuities

In a natural discontinuity, fluid flow occurs through interconnected voids between two rough rock surfaces that are in partial contact (Zimmermann et al., 1992). Fluid flow is greatest through the largest apertures, and lowest through the contact areas. As a first approximation, the fluid flow along a discontinuity is modelled as flow between two parallel plates with constant hydraulic aperture (b_h), as described by the “cubic law” (Snow, 1965):

$$q_f = \frac{b_h^3 w \rho_w g}{12\mu} \Delta H \quad (12)$$

where q_f is the flow rate per unit width (w), μ is the fluid dynamic viscosity, and ΔH is the hydraulic head gradient.

The transient fluid flow in a discontinuity with uniform hydraulic aperture is modelled using the diffusivity equation written in terms of the hydraulic head (H):

$$\frac{\partial H}{\partial t} = D_h \nabla^2 H \quad (13)$$

where ∇^2 is the Laplacian, t is the time, and D_h is the scalar hydraulic diffusivity (Hummel and Müller, 2009), which is defined by:

$$D_h = \frac{K}{Z_i} = \frac{T}{Z} \quad (14)$$

where Z_i is intrinsic storativity, Z is the increase in the weight of fluid stored per unit area of a discontinuity, K is hydraulic conductivity, and T_g is the rate at which groundwater flows horizontally (transmissivity) (Cappa et al., 2008; Domenico and Schwartz, 1997). The latter is defined according to the parallel plate flow concept as:

$$T_g = \frac{w\rho_w g}{12\mu} \left[b_{hi} + \frac{\sigma'_{ni}}{k_{nif}^{1/3}} \left(1 - \frac{\sigma'_{ni}}{\sigma'_n} \right) \right]^3 \quad (15)$$

where k_{nif} is the initial discontinuity normal stiffness, σ'_{ni} is the initial effective normal stress, b_{hi} is the initial hydraulic aperture at the initial effective stress, and σ'_n is the effective normal stress.

Elastic hydromechanical behaviour of rock discontinuities

The most fundamental formulation for describing the coupling between hydraulic and mechanical processes in geological media is the effective stress law developed by Terzaghi (1923) and Biot (1941). The effective stress law describes the relationship between effective normal stress (σ'_n), normal stress (σ_n) and fluid pressure (P_f):

$$\sigma'_n = \sigma_n - \alpha P_f \quad (16)$$

where α is effective stress coefficient. The latter is defined as follows (Walsh, 1981):

$$\alpha = 1 - \frac{1}{A} \frac{\partial(\rho_w g V_f)}{\partial P_f} \quad (17)$$

where A is the area of the discontinuity plane and V_f is the fluid volume between the two fracture faces.

Under normal stress, the parallel-plate flow concept is commonly used to describe the coupling between discontinuity flow and normal deformation, according to the “modified cubic law” suggested by Witherspoon et al. (1980):

$$q_f = \frac{(b_{hi} + f\Delta U_n)^3 w \rho g}{12\mu} \Delta H \quad (18)$$

where f is a factor reflecting the influence of roughness on the tortuosity of flow. This law associates the discontinuity hydraulic aperture (b_h) to the discontinuity normal displacement (U_n):

$$b_h = b_{hi} + f\Delta U_n \quad (19)$$

Discontinuity displacements are induced by a change in the effective stress field acting on the discontinuity. The relationship between stresses and discontinuity displacement is described by numerous mechanical constitutive laws (Barton et al., 1985; Goodman, 1970). The most basic relation between a change in discontinuity normal and shear displacements (respectively, noted U_n and U_s) caused by a change in effective normal (σ'_n) and shear (σ'_s) stresses is suggested by the linear equations of Goodman (1970):

$$\Delta U_n = \frac{\Delta \sigma'_n}{K_n} \quad (20)$$

$$\Delta U_s = \frac{\Delta \sigma'_s}{K_s} \quad (21)$$

where K_n and K_s are the normal and shear stiffness, respectively.

Stiffness of rock discontinuities

The normal and shear stiffness of discontinuities was estimated from the rock mass modulus, intact rock modulus and discontinuity spacing. If we assume that the deformability of a rock mass is due to the deformability of the intact rock and the deformability of the discontinuity in the rock mass, then:

$$\frac{1}{E_m} = \frac{1}{E_i} + \frac{1}{K_n L} \quad (22)$$

where E_m is rock mass modulus, E_i is intact rock modulus and L is mean discontinuity spacing. This assumes a single discontinuity set with an average spacing L , oriented perpendicularly to the direction of loading. This can be re-arranged to account for the discontinuity normal stiffness (Barton, 1972):

$$K_n = \frac{E_i E_m}{L(E_i - E_m)} \quad (23)$$

The same reasoning can be used to derive an expression for the discontinuity shear stiffness:

$$K_s = \frac{G_i G_m}{L(G_i - G_m)} \quad (24)$$

where G_m is rock mass shear modulus, G_i is intact rock shear modulus and L is mean discontinuity spacing.

Dissolution of rock discontinuities

Discontinuity dissolution cannot be explicitly modelled with a Distinct Element Model. This process was therefore simulated by assuming that the change in discontinuity volume with time ($\Delta V(t)$) is equivalent to the volume of dissolved mineral (V_m), which was calculated as follows (adapted from Garcia-Rios et al., 2015):

$$V_m(t) = v_m Q \int_{t=0}^{t'=t} \beta^{-1} C_j(t_s) dt' \quad (25)$$

where v_m is the molar volume of mineral (m^3/mol), β is the stoichiometric coefficient of element j in the mineral, C_j is the concentration of the element j from dissolved mineral and t_s is the sampling time.

Matrix fluid flow in clay

Richards' equation (List and Radu, 2016) is used to calculate the rate of water infiltrated into the Blue Clay Formation. The matrix flow has been modelled using the fluid continuity equation:

$$\frac{n}{K_f} \frac{\partial u_w}{\partial t} = (-q_{i,i} + q_v) - \frac{\partial \varepsilon}{\partial t} \quad (26)$$

where K_f is fluid bulk modulus, n is porosity, u_w is pore pressure, ε is mechanical volumetric strains, $q_{i,i}$ is the specific discharge vector, and q_v is the volumetric fluid source intensity. Equation (26) relies on a finite-difference nodal formulation of the fluid continuity equation.

Creep in clay

The soft soil creep model is characterised by stress-dependent stiffness, a distinction between primary loading and unloading-reloading, secondary time-dependent compression, aging of pre-consolidation stress, and failure behaviour according to the Mohr-Coulomb criterion (Matsui and Abe, 1998; Stolle et al., 1997; Vaid and Campanella, 1977). The main assumption is that the elastic strains are instantaneous and plastic strains are only viscous and will develop over time. The viscoplastic strains are in development throughout the entire time, but the rate at which they develop will depend on a number of factors, as presented in the following equation:

$$\boldsymbol{\varepsilon}_{ij} = \boldsymbol{\varepsilon}_{ij}^e + \boldsymbol{\varepsilon}_{ij}^c \quad (27)$$

where $\boldsymbol{\varepsilon}_{ij}$ is the creep tensor, $\boldsymbol{\varepsilon}_{ij}^e$ is the elementary strain, and $\boldsymbol{\varepsilon}_{ij}^c$ is the creep strain tensor. The latter is defined as follows (Roscoe and Burland, 1968):

$$\boldsymbol{\varepsilon}_{ij}^c = \left(\frac{\partial P^{eq}}{\partial P} \right) \frac{\mu^*}{t_{day}} \left(\frac{P^{eq}}{P_p^{eq}} \right)^{\frac{\lambda^* - k^*}{\mu^*}} \left(\frac{\partial P^{eq}}{\partial \sigma_{ij}} \right) \quad (28)$$

where λ^* and k^* are the modified compression and swelling indices, μ^* is the modified creep index, t_{day} is one day and P_p^{eq} is the generalised equivalent pre-consolidation pressure. P^{eq} is a stress measure defined by the overconsolidation ratio (*OCR*) and defined as follows (Caspard et al., 2004):

$$P^{eq} = OCR \times P_p^{eq} \quad (29)$$

Mayne (1991) proposed a method for estimating OCR by combining the theories of cavity expansion and critical state soil mechanics:

$$OCR = 2 \left[\frac{1}{1.95M + 1} \left(\frac{q_t - u_w}{\sigma'_{v0}} \right) \right]^{1/\Lambda} \quad (30)$$

where M is the slope of critical state line, $q_t = 2\bar{\gamma} \times ds$ (where $\bar{\gamma}$ is the average total unit weight of soil and ds is soil depth), σ'_{v0} is total stress in the vertical direction and $\Lambda = 1 - k^*/\lambda^*$.

The relationship between the modified compression and swelling indices with the original ones, and the one dimensional compression and swelling C_c and C_r , can be defined by:

$$\lambda^* = \frac{\lambda}{1+n} = \frac{C_c}{2.3(1+n)} \quad (31)$$

$$k^* = \frac{k_{sw}}{1+n} \approx \frac{2C_r}{2.3(1+n)} \quad (32)$$

$$P^{eq} = \tau_p + \frac{\tau_q^2}{M^2(\tau_p + c \cot \varphi)} \quad (33)$$

where λ is standard clay compression index, k_{sw} is standard swelling index, τ_p and τ_q are stress invariants calculated based on the current stress state, and c and φ are the cohesion and friction angle of the material, which are used to define its shear strength with a Mohr-Coulomb criterion.

Sliding of rock body on clay

The force acting on a rock body on clay can be specified according to the following (Hoek and Bray, 1991):

$$\text{Force} = (V_p \cos y_p + W_b \sin y_p) - (c'(H - z_t) \csc y_p + (W_b \cos y_p - U_p - V_p \sin y_p) \tan \varphi) \quad (34)$$

where c' is effective cohesion, y_p is dip of slide plane, W_b is the weight of the block, U_p is uplift force along slide plane due to vertical creep strain, V_p is the force due to water pressure in a tension crack in the horizontal creep strain direction, H is slope height, and z_t is tension crack depth.

b. Model parameters

The geometry, geological and geotechnical data for the model were derived from the orthophotos, digital elevation models, field observations, geotechnical and hydraulic property measurements, and near-surface geophysical surveys at Gnejna Valley. The domain's dimensions are 1000 m by 500 m by 40 m (Figure 1C). The 40 m high vertical dimension is divided into 13 m of Tal-Pitkal Member, 12 m of Mtarfa Member and 15 m of Blue Clay.

Joints in the Upper Coralline Limestone members have a spacing of 5 m, and dip angles and directions of 90° and 0°, and of 90° and 270°, respectively. The overall slope gradient is 2°.

The rate of groundwater discharge was derived from the hydrological model (section 3.1) and is equivalent to $0.01 \text{ m}^3 \text{ s}^{-1}$. We assume that the perched groundwater system feeding the natural spring at Gnejna Valley is an open system in equilibrium.

c. Simulations of detachment at limestone wall

The numerical simulations of detachment explored the following processes:

- (1) widening of valley head-orthogonal joints and fractures by fluid pressure and dissolution, which consequently reduces Upper Coralline Limestone's rock mass strength;
- (2) creep of Blue Clay, which leads to loss of support at the base of the valley head;
- (3) combination of (1) and (2).

Four modes of groundwater seepage across the fault damage zone were simulated:

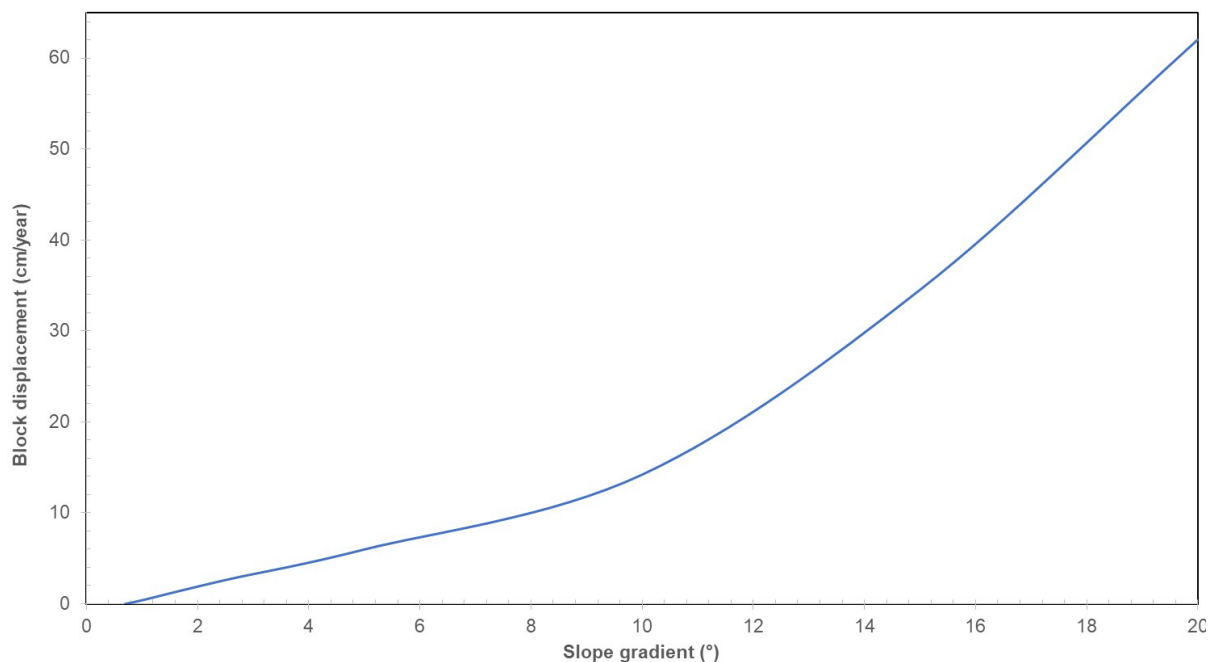
1. point seepage;
2. no change (i.e. uniform seepage);
3. linear decrease in seepage, changing from maximum at fault at the centre, to zero at the boundaries of the fault damage zone;
4. exponential decrease in seepage, changing from maximum at fault at the centre, to zero at the boundaries of the fault damage zone.

Modes 2-4 were implemented by including fractures across a 250 m wide fault damage zone (Figure 1C).

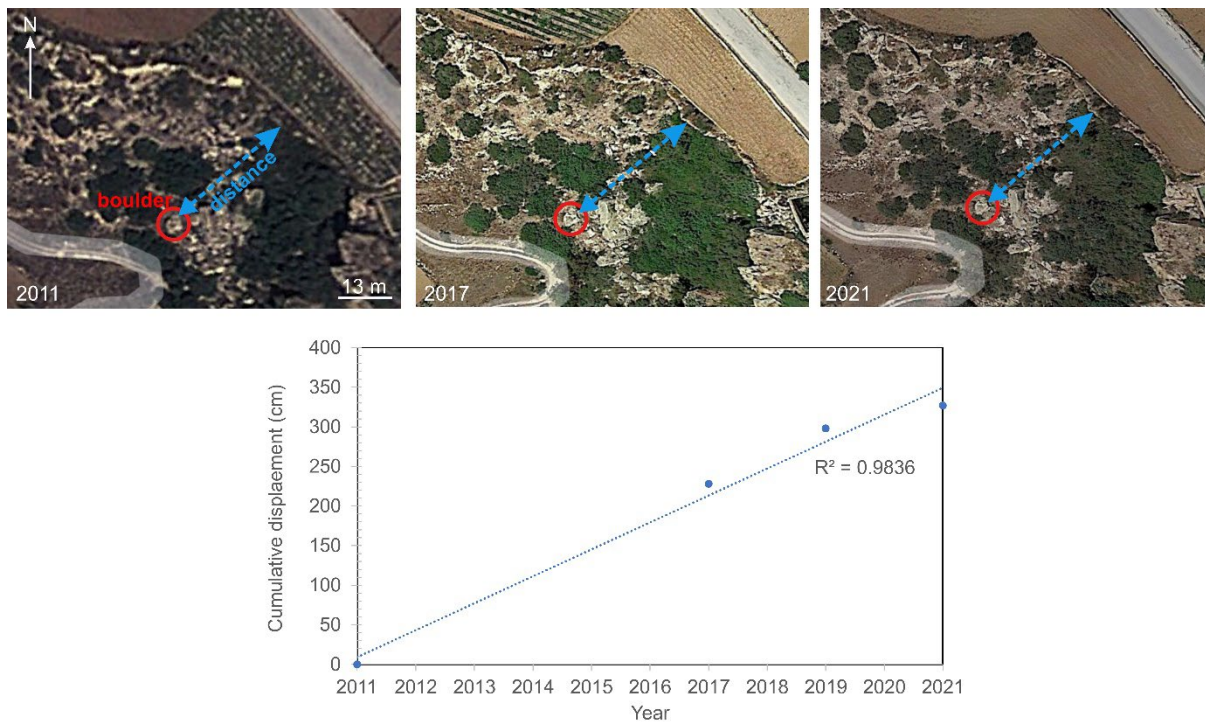
The model was run by executing a series of 45000 calculation cycles. In this study, each cycle was composed of a sequence of operations based on one year of groundwater flow.

d. Simulations of block evacuation on clay valley bed

The above Distinct Element Model was also used to simulate the evacuation of failed Upper Coralline Limestone boulders by creep and sliding. Block displacement rate was estimated for Upper Coralline Limestone blocks with a diameter of 1.5 m for different slope gradients (Figure S6).



We were able to test the accuracy of our model at estimating Upper Coralline Limestone boulder displacement rate by measuring the displacement of a boulder using Google Earth images for the period 2011-2021 (Figure S7). The Upper Coralline Limestone boulder, with dimensions of 5.4 m by 4.0 m by 2.5 m, is located on Blue Clay with a slope gradient of 20° on the northern edge of the head of Gnejna Valley. The displacement was measured with respect to the nearest limestone wall. The mean displacement rate estimated from these measurements was 32 cm per year (Figure S7), whereas our model's estimate was 31 cm per year.



References cited:

- Barton, N., and Choubey, V., 1977, The shear strength of rock joints in theory and practice: *Rock Mechanics*, v. 10, p. 1-54.
- Barton, N. R., 1972, A model study of rock-joint deformation: *International Journal of Rock Mechanics and Mining Sciences*, v. 9, p. 579-602.
- Barton, N. R., Bandis, S., and Bakhtar, K., 1985, Strength, deformation, and conductivity coupling of rock joints: *International Journal of Rock Mechanics and Mining Sciences*, v. 22, p. 121-140.
- Biot, M. A., 1941, General theory of three-dimensional consolidation: *Journal of Applied Physics*, v. 12, p. 144-164.
- Cappa, F., Guglielmi, Y., Turqvist, J., Tsang, C. F., and Thoraval, A., 2008, Estimation of fracture flow parameters through numerical analysis of hydromechanical pressure pulses: *Water Resources Research*, v. 44, p. W11408.
- Caspard, E., Rudkiewicz, J. L., Eberli, G. P., Brosse, E., and Renard, M., 2004, Massive dolomitization of a Messinian reef in the Great Bahama Bank: a numerical modelling evaluation of Kohout geothermal convection: *Geofluids*, v. 4, no. 1, p. 40-60.
- Chen, A., Darbon, J., and Morel, J.-M., 2014, Landscape evolution models: A review of their fundamental equations: *Geomorphology*, v. 219, p. 68-86.
- Chow, V. T., 1959, *Open Channel Hydraulics*, New York, McGraw-Hill Book Co., 680 p.:
- Constable, S. C., Parker, R. L., and Constable, C. G., 1987, Occam's inversion: A practical algorithm for generating smooth models from EM sounding data: *Geophysics*, v. 52, p. 289-300.
- Copernicus, 2018, CORINE Land Cover, Volume 2021.

- Desilets, D., Zreda, M., Almasi, P. F., and Elmore, D., 2006, Determination of cosmogenic ^{36}Cl in rocks by isotope dilution: innovations, validation and error propagation: *Chemical Geology*, v. 233, no. 3, p. 185-195.
- Domenico, P. A., and Schwartz, F. W., 1997, *Physical and Chemical Hydrogeology*, Chichester, John Wiley, 528 p.:
- Galdies, C., 2011, *The Climate of Malta: Statistics, Trends and Analysis*: National Statistics Office.
- Garcia-Rios, M., Luquot, L., Soler, J. M., and Cama, J., 2015, Influence of the flow rate on dissolution and precipitation features during percolation of CO_2 -rich sulfate solutions through fractured limestone samples: *Chemical Geology*, v. 414, p. 95-108.
- Goodman, R. E., Deformation of joints, *in* *Proceedings Determination of the in-situ modulus of deformation of rock*, Denver, 1970, Volume 477, ASTM Special Technical Publications, p. 174-196.
- Hoek, E., and Bray, J. W., 1991, *Rock Slope Engineering*, New York, Elsevier Science Publishing, 358 p.:
- Hummel, N., and Müller, T. M., 2009, Microseismic signatures of non-linear pore-fluid pressure diffusion: *Geophysical Journal International*, v. 179, no. 3, p. 1558-1565.
- ISRM, 1978, Suggested methods for the quantitative description of discontinuities in rock masses: *International Journal of Rock Mechanics and Mining Sciences and Geomechanics Abstracts*, v. 15, p. 319-368.
- , 1985, Suggested methods for determining point load strength: *International Journal of Rock Mechanics and Mining Sciences and Geomechanics Abstracts*, v. 22, p. 51-62.
- Kaufmann, G., and Braun, J., 2001, Modelling karst denudation on a synthetic landscape: *Terra Nova*, v. 13, no. 5, p. 313-320.

- Komar, P. D., 1988, Sediment transport by floods, *in* Baker, V. R., Kochel, R. C., and Patton, P. C., eds., *Flood Geomorphology*: New York, Wiley-Interscience, p. 97-111.
- List, F., and Radu, F. A., 2016, A study on the iterative methods for solving Richards' equation: *Computational Geosciences*, v. 20, p. 341-353.
- Marquardt, D. W., 1963, An algorithm for least squares estimation of nonlinear parameters: *Journal of the Society for Industrial and Applied Mathematics*, v. 11, p. 431-441.
- Marrero, S. M., Phillips, F. M., Borchers, B., Lifton, N., Aumer, R., and Balco, G., 2016a, Cosmogenic nuclide systematics and the CRONUScale program: *Quaternary Geochronology*, v. 31, p. 160-187.
- Marrero, S. M., Phillips, F. M., Caffee, M. W., and Gosse, J. C., 2016b, CRONUS-Earth cosmogenic ^{36}Cl calibration: *Quaternary Geochronology*, v. 31, p. 199-219.
- Matsui, T., and Abe, N., Verification of elasto-viscoplastic model of normally consolidated clays in undrained creep, *in* *Proceedings 6th International Conference on Numerical Methods in Geomechanics 1998*, Volume 1, p. 453-459.
- Mayne, P. W., 1991, Determination of OCR in clays by piezocone tests using cavity expansion and critical state concepts: *Soil and Foundations*, v. 31, no. 2, p. 65-76.
- Micallef, A., Foglini, F., Le Bas, T., Angeletti, L., Maselli, V., Pasuto, A., and Taviani, M., 2013, The submerged paleolandscape of the Maltese Islands: Morphology, evolution and relation to Quaternary environmental change: *Marine Geology*, v. 335, p. 129-147.
- Phillips, J. V., and Tadayon, S., 2006, Selection of Manning's Roughness Coefficient for Natural and Constructed Vegetated and Non-Vegetated Channels, and Vegetation Maintenance Plan Guidelines for Vegetated Channels in Central Arizona, 2006-5108.
- Sander, O., 2020, DUNE — The Distributed and Unified Numerics Environment, Germany, Springer International Publishing.

- Schwartz, F. W., and Zhang, H., 2003, Fundamentals of Groundwater, New York, John Wiley & Sons.
- Snow, D. T., 1965, A parallel plate model of fractured permeable media [PhD: University of California, Berkeley.
- Stolle, D., Bonnier, P., and Vermeer, P., 1997, A soft soil model and experiences with two integration schemes: Numerical Models in Geomechanics, v. 1, no. 12, p. 123-128.
- Stone, J. O., 2000, Air pressure and cosmogenic isotope production: Journal of Geophysical Research: Solid Earth, v. 105, no. B10, p. 23753-23759.
- Terzaghi, K., 1923, Die berechnung der durchlässigkeitsziffer des tones aus dem verlauf spannungserscheinungen: Wien, Sitzungsberichte, Mathematisch-naturwissenschaftliche Klasse, v. 142, no. 3/4, p. 125-138.
- Uppala, S. M., Kållberg, P. W., Simmons, A. J., Andrae, U., Bechtold, V. D. C., Fiorino, M., Gibson, J. K., Haseler, J., Hernandez, A., Kelly, G. A., Li, X., Onogi, K., Saarinen, S., Sokka, N., Allan, R. P., Andersson, E., Arpe, K., Balmaseda, M. A., Beljaars, A. C. M., Berg, L. V. D., Bidlot, J., Bormann, N., Caires, S., Chevallier, F., Dethof, A., Dragosavac, M., Fisher, M., Fuentes, M., Hagemann, S., Hólm, E., Hoskins, B. J., Isaksen, I., Janssen, P. A. E. M., Jenne, R., McNally, A. P., Mahfouf, J.-F., Morcrette, J.-J., Rayner, N. A., Saunders, R. W., Simon, P., Sterl, A., Trenberth, K. E., Untch, A., Vasiljevic, D., Viterbo, P., and Woollen, J., 2005, The ERA-40 re-analysis: Quarterly Journal of the Royal Meteorological Society, v. 131, no. 612, p. 2961-3012.
- Vaid, Y., and Campanella, R., 1977, Time-dependent behaviour of undisturbed clay: Journal of Geotechnical Engineering, v. 103, no. 7, p. 693-709.
- Walsh, J. B., 1981, Effect of pore pressure and confining pressure on fracture permeability: International Journal of Rock Mechanics and Mining Sciences, v. 18, p. 429-435.

Witherspoon, P. A., Wang, J. S. Y., Iwai, K., and Gale, J. E., 1980, Validity of cubic law for fluid flow in a deformable rock fracture: *Water Resources Research*, v. 16, no. 6, p. 1016-1024.

Zimmermann, R. W., Chen, D. W., and Cook, N. G. W., 1992, The effect of contact area on the permeability of fractures: *Journal of Hydrology*, v. 139, p. 79-96.